Near-field radiation between graphene-covered carbon nanotube arrays

Richard Z. Zhang, Xianglei Liu, and Zhuomin M. Zhang

Citation: AIP Advances **5**, 053501 (2015); doi: 10.1063/1.4913993
View online: http://dx.doi.org/10.1063/1.4913993
View Table of Contents: http://aip.scitation.org/toc/adv/5/5
Published by the American Institute of Physics

Articles you may be interested in

Near-field thermal radiation between hyperbolic metamaterials: Graphite and carbon nanotubes
Applied Physics Letters **103**, 213102 (2013); 10.1063/1.4832057

Near-field radiative heat transfer between doped-Si parallel plates separated by a spacing down to 200 nm
Applied Physics Letters **109**, 203112 (2016); 10.1063/1.4967384

Graphene-assisted near-field radiative heat transfer between corrugated polar materials
Applied Physics Letters **104**, 251911 (2014); 10.1063/1.4885396

Giant enhancement of nanoscale thermal radiation based on hyperbolic graphene plasmons
Applied Physics Letters **107**, 143114 (2015); 10.1063/1.4932958

Super-Planckian near-field thermal emission with phonon-polaritonic hyperbolic metamaterials
Applied Physics Letters **102**, 131106 (2013); 10.1063/1.4800233

Near-field radiative thermal transport: From theory to experiment
AIP Advances **5**, 053503 (2015); 10.1063/1.4919048

AIP ADVANCES **5**, 053501 (2015)

Near-field radiation between graphene-covered carbon nanotube arrays

Richard Z. Zhang, Xianglei Liu, and Zhuomin M. Zhang[a]
George W. Woodruff School of Mechanical Engineering, Georgia Institute of Technology, Atlanta, Georgia 30332, USA

(Received 3 December 2014; accepted 29 December 2014; published online 27 February 2015)

It has been shown that at small separation distances, thermal radiation between hyperbolic metamaterials is enhanced over blackbodies. This theoretical study considers near-field radiation when graphene is covered on the surfaces of two semi-infinite vertically aligned carbon nanotube (VACNT) arrays separated by a sub-micron vacuum gap. Doped graphene is found to improve photon tunneling in a broad hyperbolic frequency range, due to the interaction with graphene-graphene surface plasmon polaritons (SPP). In order to elucidate the SPP resonance between graphene on hyperbolic substrates, vacuum-suspended graphene sheets separated by similar gap distances are compared. Increasing the Fermi energy through doping shifts the spectral heat flux peak toward higher frequencies. Although the presence of graphene on VACNT does not offer huge near-field heat flux enhancement over uncovered VACNT, this study identifies conditions (i.e., gap distance and doping level) that best utilize graphene to augment near-field radiation. Through the investigation of spatial Poynting vectors, heavily doped graphene is found to increase penetration depths in hyperbolic modes and the result is sensitive to the frequency regime. This study may have an impact on designing carbon-based vacuum thermophotovoltaics and thermal switches. © *2015 Author(s). All article content, except where otherwise noted, is licensed under a Creative Commons Attribution 3.0 Unported License.* [http://dx.doi.org/10.1063/1.4913993]

I. INTRODUCTION

Flat surfaces that are separated by a sub-micron vacuum gap can provide radiative transfer exceeding that between blackbodies in the far field, due to the increased tunneling probability of evanescent waves.[1–3] The appreciation for the distinctive characteristics that near-field radiation offers is prevalent in engineering more effective multi-component thermophotovoltaic cells,[4–6] thermal modulators or rectifiers,[7,8] and many other nanoscale components that require precision control of thermal states. In the near field, the critical radiative characteristic is what lies beneath the surface, the frequency-dependent dielectric permittivity of the medium. Over simple bulk materials, anisotropic uniaxial metamaterials can exhibit low-loss hyperbolic dispersion in which resonance-free and broad evanescent modes exist.[9–13] One such material that exhibits hyperbolic dispersion from the mid- to far-infrared region is vertically aligned carbon nanotube (VACNT) arrays.[14,15]

The discovery and characterization of single-layer carbon atom sheets, called graphene, have opened doors to tailoring electromagnetic interactions in nanoscale devices.[16–19] In short, the low scattering and high mobility transport of graphene's charge carriers, tunable through either voltage gating or doping, enables quantum state superconductivity in an atomically thin sheet from the near-infrared to low-terahertz regimes.[20–25] Especially with the high fidelity processes of isolating graphene in the electronically distinct single layer form,[26,27] its potential usage in nanomaterial optical cloaking,[28] tunable and transparent plasmonic metasurfaces,[29,30] and other novel photonic

[a]Corresponding author. Email: zhuomin.zhang@me.gatech.edu. Tel: 404-385-4225.

 ©Author(s) 2015

applications is now realized.[19,31] Naturally, due to the chemical and crystallographic matching between carbon nanotubes (CNT) and graphene,[32–35] the hybridization of the two certainly deserves attention.

When doped graphene sheets are placed on VACNT substrates, which are separated by a small vacuum gap, will the presence of graphene improve or reduce heat transfer? The objective of this study is to investigate the near-field heat flux in accordance with the fluctuation-dissipation theorem through modeling of the electronic properties of VACNT and graphene in a broad frequency range. While both VACNT and graphene have contributing tunneling modes, the combination of which may not be so intuitive. The tunable parameters of graphene are also introduced to illustrate a best possible scenario for heat flux enhancement. A unique aspect of this study is the determination of the Poynting vector (or heat flux) variation from the depths of the graphene-covered VACNT emitter, through the vacuum, and under the VACNT receiver. This study elucidates the hybridization between the tunable resonant mode contributions from doped graphene and the intrinsic hyperbolic nature of VACNT.

II. MODELING AND METHODS

The schematic for calculating near-field radiative transfer is depicted in Figure 1, which consists of two semi-infinite VACNT arrays separated by a submicron vacuum gap. In the cases of interest, each VACNT array is covered by a single-layer graphene sheet. Unlike continuous structures such as pillared graphene where phonon scattering dominates near the graphene-CNT junctions,[34,36] the graphene sheet is assumed to not bond or interact with the CNT substrate, which could degrade their unique electronic properties.[37] In order to maximize radiative heat flux, graphene doping levels or chemical potentials are set equal on both the emitter and receiver.[38]

To model the sheet conductivity of a single-layer graphene in the infrared, both intraband and interband contributions need to be considered. The intraband conductivity can be described by a Drude-like term,

$$\sigma_{\text{Drude}}(\mu,\omega,T) = \frac{i}{\omega + i/\tau}\frac{e^2}{\pi\hbar^2}2k_BT\ln\left[2\cosh\left(\frac{\mu}{2k_BT}\right)\right] \tag{1}$$

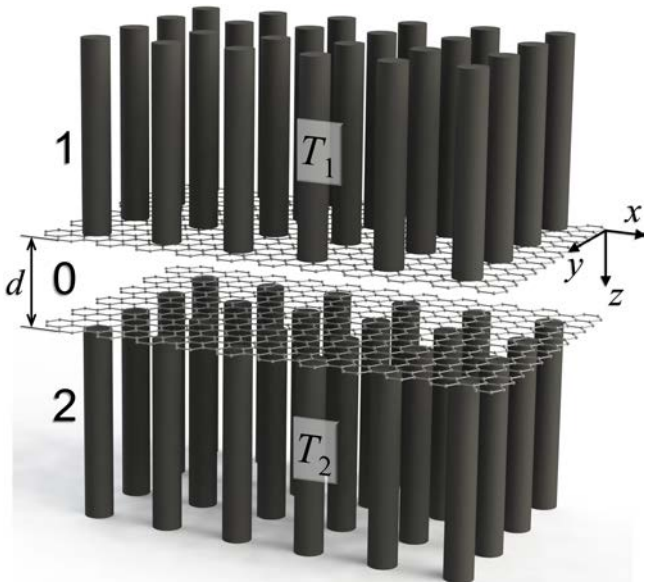

FIG. 1. 3D illustration of semi-infinite VACNT media covered with single-layer graphene sheets. The vacuum gap (medium 0), indicated by dimension d, must be no smaller than the inter-CNT spacings. The emitter (medium 1) is set at temperature T_1, and the receiver (medium 2) is at T_2.

where μ is the Fermi energy or chemical potential, which can be tuned by doping graphene with impurities, ω the frequency, and T the absolute temperature.[22] In the limit whereby $|\mu| \gg k_B T$, the latter term $2k_B T \ln[2\cosh(\mu/2k_B T)]$ in Eq. (1) can be approximated as μ. The DC relaxation time τ due to carrier-impurity scattering typically ranges from 10^{-13} s to 10^{-12} s and increases with higher chemical potential[16,20,23,39–41] For Eq. (1) to be valid, the scattering rate τ^{-1} should be smaller than the optical frequency ω.[22,42] This criterion is satisfied since the majority of thermal radiation near room temperature falls in the mid-infrared region.

The interband conductivity for direct electron transitions at non-zero temperatures is modeled using

$$\sigma_{\text{Inter}}(\mu,\omega,T) = \frac{e^2}{4\hbar}\left[G\left(\frac{\hbar\omega}{2}\right) + i\frac{4\hbar\omega}{\pi}\int_{\eta=0}^{\infty}\frac{G(\eta)-G(\hbar\omega/2)}{(\hbar\omega)^2-4\eta^2}d\eta\right] \tag{2}$$

where $G(\eta) = \sinh(\eta/k_B T)/[\cosh(\eta/k_B T)+\cosh(\mu/k_B T)]$ is the difference function from the Fermi-Dirac distribution.[1,22,42] Numerically, the integrating variable η is taken from 0 to 10μ, which provides a sufficient upper bound at near room temperatures. Toward high frequencies, the interband conductivity approaches the universal 2D conductivity for undoped graphene, such that $\sigma_0 \equiv \sigma(\omega \to \infty) = e^2/4\hbar$.[21,25] The surface conductivity of graphene is calculated by the sum, $\sigma = \sigma_{\text{Drude}} + \sigma_{\text{Inter}}$.

Figure 2 shows the graphene conductivity relative to σ_0 for three selected chemical potentials over the prescribed frequency range, both of which are used in the figures and discussions from here on. The lowest chemical potential, $\mu = 0.1$ eV (blue dashed line), has a dip in the real component of conductivity at $\omega \approx 1.5 \times 10^{14}$ rad/s, shown in Fig. 2(a). This dip corresponds to the onset of the interband transition at $\omega = 2\mu$, whereby the imaginary component, as seen in Fig. 2(b), reaches a minimum.[21,43] Meanwhile, for higher chemical potentials, the Drude conductivity dominates since the interband transition occurs in the frequency range outside of interest. The upper-bound frequency is determined by the optical phonon frequency $\hbar\omega_{op} \approx 0.2$ eV($\omega_{op} \approx 3 \times 10^{14}$ rad/s). Above such frequency, optical phonon emission alongside electron-hole pair coupling is significant.[39] Here, the relaxation time is overcome by electron-phonon scattering and high plasmon losses, resulting in as large as an order magnitude reduction. The lower bound frequency is set to $\omega = 3 \times 10^{12}$ rad/s. This broad frequency range includes most of the thermal radiation emitted at 300 K.

The modeling of the semi-infinite VACNT media is achieved by applying the anisotropic graphite optical properties to the effective medium theory (EMT) based on the Maxwell-Garnett approximation.[44–46] Using a default volume filling ratio of $f = 0.05$ and assuming an average CNT filament diameter of 30 nm,[47,48] EMT is valid for near-field vacuum gap distances greater than the lattice constant divided by π ($d \approx 38$ nm).[10,49] In addition, an alignment factor (set as $x = 0.98$)

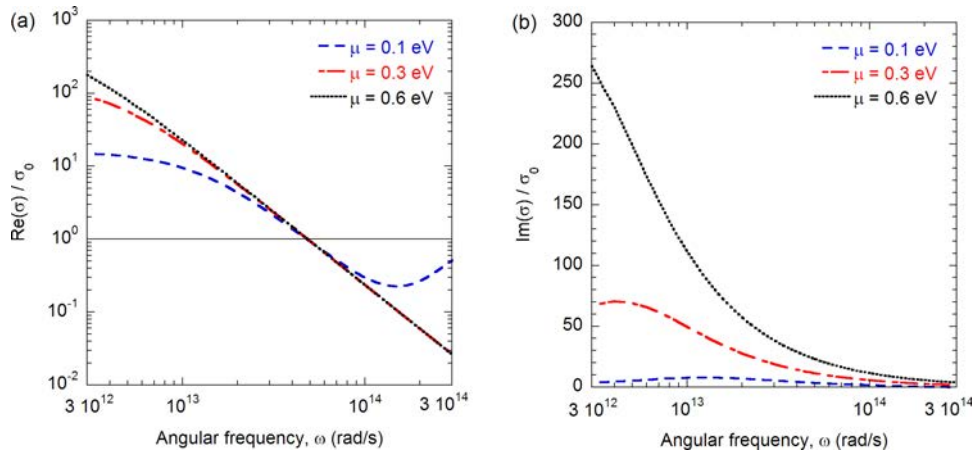

FIG. 2. Conductivity of graphene divided by the universal conductivity of undoped graphene, σ_0. The real part is shown in (a), and imaginary part in (b).

is utilized to account for random tilting and entanglements in the VACNT array.[50] The relative permittivities of the VACNT array are expressed as ε_O and ε_E, for ordinary wave (electric field perpendicular to z-axis) and extraordinary wave (electric field parallel to z-axis), respectively.

The near-field heat flux between two homogeneous media, from derivations of fluctuational electrodynamics, is given by

$$Q(\beta,\omega,T_1,T_2) = \frac{1}{4\pi^2}\int_0^\infty [\Theta(\omega,T_1)-\Theta(\omega,T_2)]\,d\omega \int_0^\infty \beta \sum_{j=s,p} \xi_j(\omega,\beta)d\beta \tag{3}$$

where the Planck oscillator function Θ is a function of frequency ω and the emitter or receiver temperature.[3,10,49] In the present study, the emitter and receiver temperatures are set to $T_1 = 300$ K and $T_2 = 0$ K, respectively. However, in calculating the dielectric functions of VACNT and conductivities of graphene, all properties are evaluated at 300 K. The second term integrates the energy transmission coefficient $\xi(\omega,\beta)$ over the lateral wavevector β for both TE-wave (s-polarization) and TM-wave (p-polarization). The energy transmission coefficient contains contributions from propagating modes ($\beta < k_0$) and evanescent modes ($\beta > k_0$) as given below,[10,38]

$$\xi_j(\omega,\beta) = \begin{cases} \dfrac{\left(1-\left|r_{01}^j\right|^2\right)\left(1-\left|r_{02}^j\right|^2\right)}{\left|1-r_{01}^j r_{02}^j e^{-2i\gamma d}\right|^2}, & \beta < k_0 \\ \dfrac{4\mathrm{Im}\left(r_{01}^j\right)\mathrm{Im}\left(r_{02}^j\right)e^{-2\mathrm{Im}(\gamma)d}}{\left|1-r_{01}^j r_{02}^j e^{-2i\gamma d}\right|^2}, & \beta > k_0 \end{cases} \tag{4}$$

where $\gamma = \sqrt{k_0^2-\beta^2}$ is the z-component wavevector, and k_0 is the magnitude of the wavevector in vacuum. For graphene-covered uniaxial medium, the Fresnel reflection coefficients at the two interfaces ("01" is between vacuum and emitter, and "02" is between vacuum and receiver) are given by[14,51]

$$r^s = \frac{\gamma - k_z^s - \sigma\omega\mu_0}{\gamma + k_z^s + \sigma\omega\mu_0} \tag{5}$$

$$\text{and} \quad r^p = \frac{\varepsilon_O\gamma - k_z^p + \sigma k_z^p\gamma/\omega\varepsilon_0}{\varepsilon_O\gamma + k_z^p + \sigma k_z^p\gamma/\omega\varepsilon_0} \tag{6}$$

Here, $k_z^s = \sqrt{k_0^2\varepsilon_O - \beta^2}$ and $k_z^p = \sqrt{k_0^2\varepsilon_O - \beta^2\varepsilon_O/\varepsilon_E}$ are functions of the VACNT permittivities. For cases with no graphene covering the VACNT arrays, one can simply set $\sigma = 0$. Another way of calculating Fresnel's coefficients is to assume graphene as an ultrathin layer, and use the transfer matrix formulation as to be discussed later. The two methods yield essentially the same results.

III. RESULTS AND DISCUSSION

A. Hybridization between graphene SPP and VACNT hyperbolic modes

Figure 3 shows the near-field transmission coefficient expressed in Eq. (4), across a broad frequency and lateral wavevector range. The contour plot figures in the left column correspond to the transmission coefficient between two graphene sheets separated by a vacuum gap ($d = 100$ nm), but without substrates, called vacuum-suspended graphene. The right-side column figures describe the near-field device including the VACNT substrates from Fig. 1. The three rows are associated with different chemical potentials, $\mu = 0.1$ eV, 0.3 eV, and 0.6 eV, respectively. The purpose of illustrating the transmission coefficient of vacuum-suspended graphene is to determine the surface plasmon polariton (SPP) dispersion between graphene sheets. The coupled SPP dispersion relation is given by[14,52]

$$\frac{2\omega\varepsilon_0}{\gamma\sigma(\omega,\mu,T)} = \pm\exp(i\gamma d) - 1 \tag{7}$$

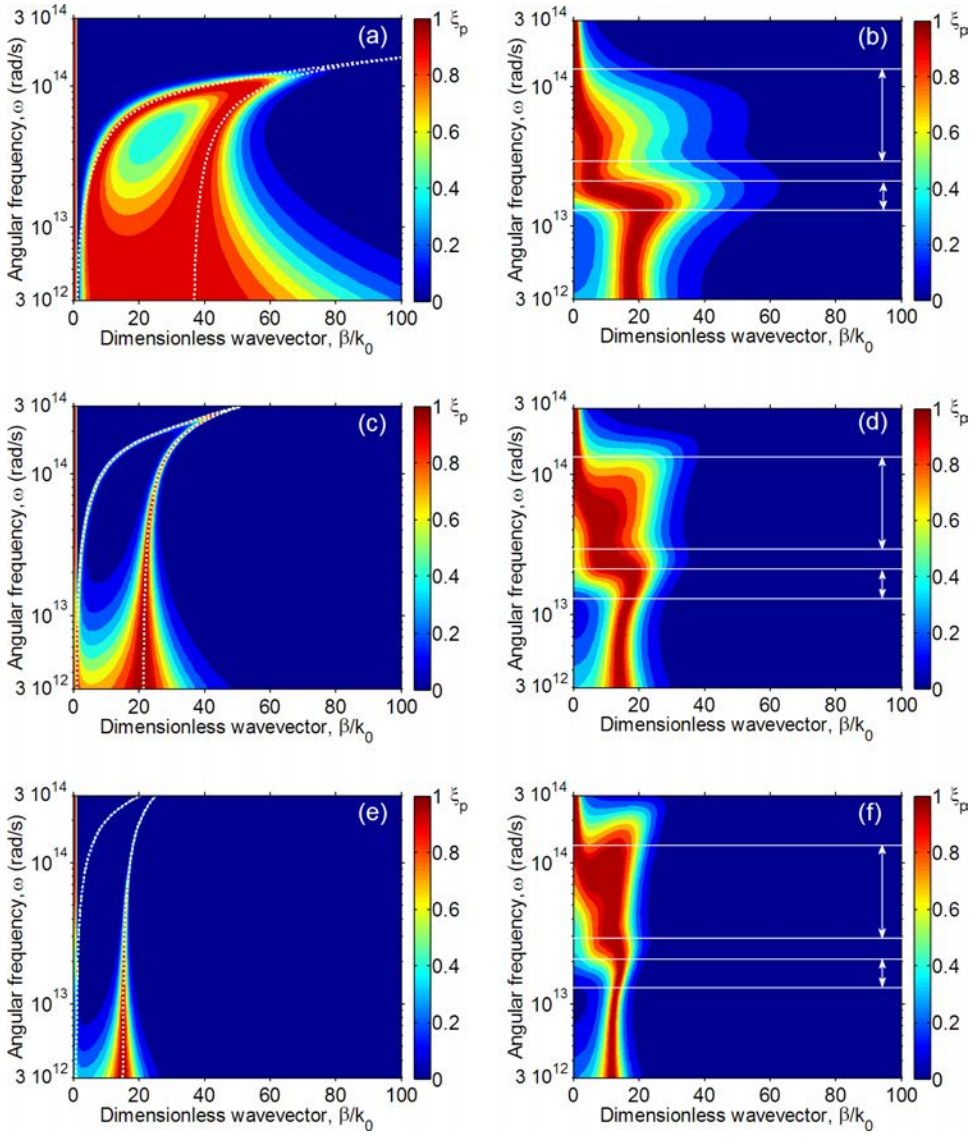

FIG. 3. Near-field tunneling transmission coefficient contours in lateral wavevector and frequency space of vacuum-suspended graphene for chemical potentials of (a) $\mu = 0.1$ eV, (c) 0.3 eV, and (e) 0.6 eV. The hybridization of graphene plasmon resonance and hyperbolic modes is observed in the graphene-covered VACNT configuration at (b) $\mu = 0.1$ eV, (d) 0.3 eV, and (f) 0.6 eV. The hyperbolic dispersion frequency regions of VACNT are denoted by the white arrows between the horizontal lines. The near-field gap distance used for this figure and every successive figure is $d = 100$ nm.

In Figs. 3(a), 3(c), and 3(e), the SPP dispersion curves or bands are drawn in dotted white lines. The symmetric band, as shown by the left-hand line, has a $\omega \propto \sqrt{\beta}$ relationship and originates close to the light line.[53] The anti-symmetric mode is represented by the right-hand line, and its resonant lateral wavevector increases inversely with the separation distance d. The two SPP mode lines merge toward high frequencies.[54]

Some notable observations on the transmission contours: For greater chemical potential, near-unity transmission in the low frequency range covers a narrow band of lateral wavevectors. This low frequency band reflects the narrowing of vacuum-suspended graphene anti-symmetric SPP dispersion. On the other hand, in the high frequency region, the band of near-unity transmission is broadened, and in the case when $\mu = 0.6$ eV, high transmission is extended to include frequencies beyond the hyperbolic band. Therefore, with higher chemical potential, the low frequency region

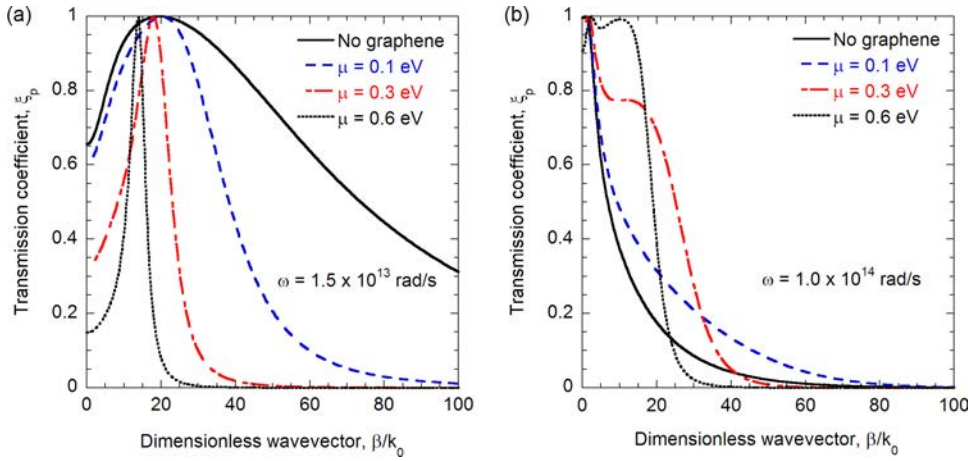

FIG. 4. The transmission coefficient between VACNT for both uncovered and graphene-covered configurations, shown at frequencies (a) $\omega = 1.5\times10^{13}$ rad/s, and (b) $\omega = 1\times10^{14}$ rad/s.

suffers decreasing number of hyperbolic modes in order to support broad near-unity transmission in the high frequency hyperbolic region. However, why do the SPP bands of weakly doped graphene exhibit less influence on the transmission contour of the hybridized structure, as such seen in Fig. 3(b)? In reference to Eq. (4), the denominator of the transmission coefficient, $1 - r_{01}^{p} r_{02}^{p} e^{-2i\gamma d}$, is found to be many orders of magnitudes smaller when the chemical potential is increased.[56,57] While weakly doped graphene shows broader near-unity transmission in the vicinity of the SPP dispersion lines, the denominator of the transmission coefficient is far from zero. When the denominator is zero, which happens to be the SPP dispersion relation given in Eq. (7), perfect SPP resonance will occur.

Figure 4 gives the transmission coefficient at $\omega = 1.5 \times 10^{13}$ rad/s and $\omega = 1.0 \times 10^{14}$ rad/s to demonstrate the tradeoffs more clearly at both a low frequency and high frequency. In Fig. 4(a), without graphene (black line), the transmission coefficient is $\xi_p \geq 0.3$ in the lateral wavevector range indicated. With graphene, the number of evanescent modes promoting high near-field transmission is reduced. Especially with high chemical potential, the peak of the lateral wavevector is shifted toward smaller values and narrowed. The trend at $\omega = 1.0 \times 10^{14}$ rad/s is quite different, as evidenced in Fig. 4(b), since graphene is able to improve the range of near-unity transmission. A "shoulder" is observed in the evanescent modes close to $\beta/k_0 = 20$ for $\mu = 0.3$ eV, and evolves into dual peaks near unity for $\mu = 0.6$ eV. One may also notice the sharp drop in ξ_p for $\beta/k_0 > 20$. Although both frequencies satisfy hyperbolic dispersion in the VACNT substrate, highly doped graphene presents strong surface plasmons that can either disrupt or add to the hyperbolic modes depending on the frequency. A complementary discussion providing more depth on mode hybridization is given in the following sections.

B. Parameters for heat flux enhancement or reduction using graphene

In this section, the encompassing effect from the transmission contours is demonstrated with near-field radiative heat flux. Eq. (3) without the integration over ω is shown in Figure 5, as the spectral heat flux in base units of W/m^2 per rad/s. Fig. 5(a) compares such spectra between uncovered VACNT and graphene-covered VACNT. Due to the large number of evanescent modes in the low frequency hyperbolic region, the spectral heat flux has a dominant peak near $\omega = 1.5 \times 10^{13}$ rad/s. In the presence of graphene, this peak is immensely curbed. By how much, the normalized cumulative heat flux from Fig. 5(b) reveals the contribution by the low frequency modes up to $\omega = 2.1 \times 10^{13}$ rad/s. The low frequency region heat flux contribution of uncovered VACNT was found to be 14%,[55] but with graphene this drastically decreases down from 2.7% to 0.7%, from low to high doping.

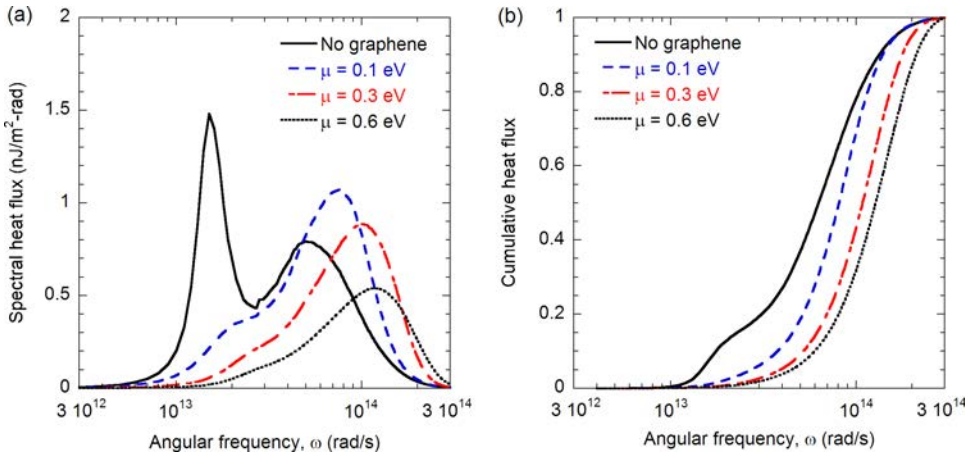

FIG. 5. (a) Spectral heat flux (nW/m^2 per rad/s) for uncovered and graphene-covered VACNT, and (b) the normalized cumulative heat flux up to the optical phonon frequency, $\omega_{op} \approx 3\times10^{14}$ rad/s.

Meanwhile, the second peak due to the high frequency hyperbolic mode is improved with some doped graphene. At $\mu = 0.1$ eV, this peak not only increases in magnitude, but also shifts toward a higher frequency. With $\mu = 0.3$ eV and onwards, the peak frequency shifts farther up, agreeing well with the interband transition shift discussed earlier. However, highly doped graphene comes at a cost, since the extent of lateral wavevectors that present non-negligible transmission ($\xi_p > 0.05$) is reduced. Even with the formation of a near-unity transmission butte that is shifted toward the high frequency, the resulting spectral heat flux is diminished. This effect occurs in doped graphene at $\mu = 0.6$ eV, where the high frequency peak becomes shorter than that for uncovered VACNT.

The integration of the spectral heat flux with frequency results in the near-field heat flux between the emitter and receiver. The enhancement of near-field radiative heat flux is demonstrated by normalizing it over the perfectly transmitting and propagating wave far-field black body heat flux (Q_{BB}). Figure 6 plots the heat flux enhancement for the two aforementioned near-field configurations with changing chemical potentials. The solid line, representing graphene-covered VACNT,

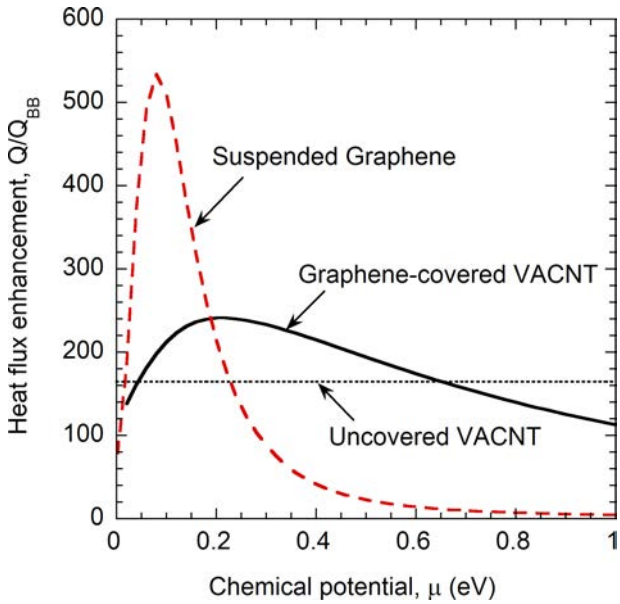

FIG. 6. Effect of graphene chemical potential on heat flux enhancement between graphene-covered VACNT, and between vacuum-suspended graphene. The horizontal dashed line represents the heat flux enhancement between uncovered VACNT.

gives the range of graphene chemical potential that results in enhancement over uncovered VACNT (horizontal dashed line). At $\mu = 0.22$ eV, the heat flux over that of far-field black body is maximized at 241 times, and over that of uncovered VACNT at 1.5 times. Agreeing with the previous discussion, too highly doped graphene ($\mu > 0.65$ eV) results in suppressed heat transfer over uncovered VACNT, at least for the 100 nm gap distance.

Just between two vacuum-suspended graphene sheets, the heat flux enhancement is maximized at a low doping level ($\mu = 0.1$ eV). Looking back at Fig. 3(a), the SPP dispersions yield high transmission coefficients throughout the contour plot. At lower chemical potential, the SPP dispersion lines approach an asymptotic cutoff frequency, in which above it no tunneling can occur. For higher chemical potential, despite the stronger resonance conditions, near-unity transmission is highly localized at the SPP modes, especially at high frequencies. In the low frequency, the anti-symmetric SPP pass-band is limited to smaller lateral wavevectors. When graphene and VACNT are combined, the chemical potential that yields the highest heat flux enhancement is increased due to the presence of underlying hyperbolic modes from the VACNT substrate. Essentially, the hybrid structure is desirable when the graphene SPP modes couple to improve the weaker hyperbolic band in high frequencies, but also allow broad non-local transmission in the low hyperbolic band frequencies and below.

Figure 7 demonstrates the effect of vacuum gap distance spacing on the near-field heat flux between graphene-covered VACNT. In the broad scheme of things, graphene slightly improves heat transfer starting at $d \approx 20$ nm, and decays with $Q \propto d^{-2}$. Below the nanometer-scale sizes, a $Q \propto d^{-1}$ relationship is observed for the graphene-covered VACNT, which matches well with a recent study.[58] Despite the counterproductive effect of graphene at these small gap distances, the validity of using EMT in near-field calculations breaks down. Considering any of the three graphene chemical potentials, the enhancement over uncovered VACNT is provided for gap distances between 91 nm and 2 μm. With the latter gap distance, the heat flux enhancement over black body is insignificant anyway. The graphene chemical potential that results in the greatest heat flux enhancement is dependent on the gap distance. In the inset of Fig. 7, at $d = 50$ nm, graphene at $\mu = 0.1$ eV is preferred over highly doped graphene. On the other end, at $d = 200$ nm, graphene doped at $\mu = 0.3$ eV and $\mu = 0.6$ eV are preferred. The understanding is that increasing the gap distance shifts the anti-symmetric SPP band toward higher lateral wavevectors. This graphene SPP

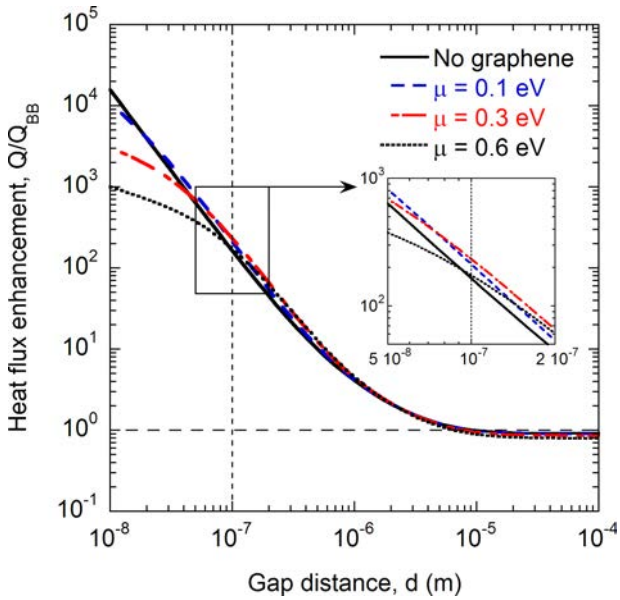

FIG. 7. Heat flux enhancement over that of black body of uncovered and graphene-covered VACNT for near-field gap distances between $d = 10$ nm and $d = 100$ μm. The inset shows the heat flux enhancement between $d = 50$ nm and $d = 200$ nm.

band, especially at stronger chemical potential, will coincide with the suppressed VACNT SPP band situated at similar lateral wavevectors. It is assumed that this SPP substitution can continue to support a broad lateral wavevector range of hyperbolic modes.

C. Graphene absorption effect on near-field Poynting vector and penetration depth

In this section, the near-field heat transport mechanism is further investigated by evaluating the electromagnetic fields in each medium. The direction of energy flow per unit projected area, the Poynting vector, is generally evaluated from the cross-product of the electric and magnetic fields.[1] The derivative of the Poynting vector with respect to z essentially shows the amount of energy absorbed or emitted per unit depth per unit time. In the vacuum gap, the Poynting vector should correspond to the near-field heat flux. But, how will SPP modes or hyperbolic modes contribute inside the emitter and receiver media? Further, the presence of graphene could improve photon penetration. The implications of greater penetration depth would suggest that thicker VACNT films are needed in order to satisfy the semi-infinite substrate assumption.[59]

The near-field TM-wave Poynting vector along the z-axis for a uniaxial medium, $\langle S_z(z,\omega,T)\rangle$, is determined by the following[59,60]

$$\langle S_z(z,\omega,T)\rangle = \frac{k_0^2\Theta(\omega,T)\beta}{2\pi^3} Re\left[i\int_z \begin{pmatrix} \varepsilon_O'' g_{\rho\rho}(\beta,\omega,z,z') h_{\theta\rho}^*(\beta,\omega,z,z') \\ +\varepsilon_E'' g_{\rho z}(\beta,\omega,z,z') h_{\theta z}^*(\beta,\omega,z,z') \end{pmatrix} dz' \right] \tag{8}$$

Here, g and h are the electric and magnetic Weyl tensor components of the dyadic Green's functions, respectively.[61,62] The Green's function components are functions of the field amplitude coefficients in each layer using the scattering matrix method, which offers better numerical stability of near-field calculations over the transfer matrix method.[60,63] In the case when graphene resides between the VACNT substrates and the vacuum gap, the dielectric permittivity based on the graphene conductivity from Eqs. (1) and (2) is

$$\varepsilon_g(\omega,\mu,T) = 1 + \frac{i\sigma(\omega,\mu,T)}{\Delta_g \omega \varepsilon_0} \tag{9}$$

where the thickness of graphene is $\Delta_g = 0.335$ nm.[38,64] Graphene as a thin slab produces nearly the same results as the surface current formulations from Eqs. (5) and (6). The dielectric permittivities of graphene, applied to the matrix method, is $\varepsilon_O = \varepsilon_g$ and $\varepsilon_E = 1$ due to the transverse current along the graphene sheet. Figure 8 demonstrates the wavevector-averaged Poynting vector $\langle S_z\rangle$ for both uncovered VACNT and graphene-covered VACNT at a vacuum gap distance of $d = 100$ nm. The spatially-dependent Poynting vector is first normalized to that in the vacuum gap, such that

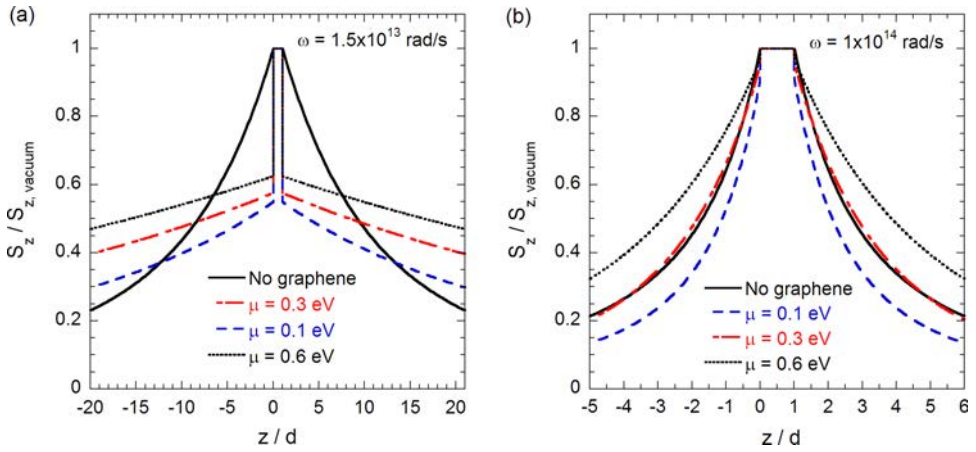

FIG. 8. Lateral wavevector-averaged longitudinal (z-direction) Poynting vector normalized to that in the vacuum gap, for hyperbolic and graphene SPP-hybridized mode frequencies (a) $\omega = 1.5\times10^{13}$ rad/s and (b) $\omega = 1\times10^{14}$ rad/s.

$\langle S_z(z)\rangle / \langle S_{z,\text{vacuum}}\rangle = 1$ when $0 < z/d < 1$. The Poynting vector profiles are evaluated at a range of evanescent wavevectors, from $\beta/k_0 = 1^+$ to $\beta/k_0 = 200$, and then averaged. The lateral wavevector modes that correspond to near-unity transmission coefficients (from Fig. 3) exert greater influence on the integrated Poynting vector.

Without the presence of graphene, no discontinuity in the Poynting vector is observed. With graphene sheets, Poynting vector discontinuities are seen near $z/d = 0^-$ and $z/d = 1^+$, precisely, inside the thin graphene-defined layers. The amount of absorption depends on both graphene chemical potential and frequency. At the low frequency regime ($\omega = 1.5 \times 10^{13}$ rad/s), in the narrowband hyperbolic dispersion that is supported by the suppressed VACNT SPP band, the presence of graphene has profound effects on energy absorption, as seen in Fig. 8(a). With increasing chemical potential, graphene is less absorbing at the surface and promotes longer penetration depth. The penetration depth (δ) is determined using

$$S_z(\delta - d) = \frac{S_z(d + \Delta_g)}{e} \tag{10}$$

The exponentially sloped decay begins at the interface between graphene and the semi-infinite VACNT substrate ($z = d + \Delta_g$). Without graphene, the penetration depth at $\omega = 1.5 \times 10^{13}$ rad/s is $\delta = 1.2$ μm. Graphene at chemical potentials of $\mu = 0.1$ eV, $\mu = 0.3$ eV, and $\mu = 0.6$ eV have penetration depths of $\delta = 3.5$ μm, $\delta = 5.6$ μm, and $\delta = 7.2$ μm, respectively. The gradual increase in the penetration depths with doping in the frequency band is due to the shift from VACNT SPP to graphene SPP, the latter situated at smaller lateral wavevectors. Accordingly, the steeper evanescent waves at small β allow maximization of the spectral penetration depth.[55,65]

At $\omega = 1.0 \times 10^{14}$ rad/s, the hyperbolic mode is weaker, resulting in smaller penetration depths. As well, the discontinuity in the Poynting vector due to the presence of graphene is reduced. Here, the penetration depth between uncovered VACNT is $\delta = 0.27$ μm. When $\mu = 0.1$ eV, the penetration depth rather decreases to $\delta = 0.21$ μm. This may be attributed to the weak graphene SPP bands that asymptote toward the large lateral wavevectors, thereby effectively adding two insulating slabs. However, at higher doping level, such as $\mu = 0.6$ eV, the penetration depth is increased to $\delta = 0.45$ μm. The increased penetration is due to the highly doped graphene that collects the dominant modes toward smaller lateral wavevectors, in agreement with the observed shape-shift seen in Fig. 4(b). For even higher frequencies (i.e. $\omega = 2 \times 10^{14}$ rad/s), the lack of intrinsic VACNT hyperbolic dispersion results in small reductions in penetration depths due to graphene (not shown).

The general increase in penetration depth due to the SPP of strongly doped graphene may impose limits on the design of VACNT substrates in near-field thermal applications. The rule of graphene over both the VACNT hyperbolic and suppressed SPP modes at frequencies below $\omega \approx 3 \times 10^{13}$ rad/s hints the need for tens-of-microns thick VACNT substrates for far-infrared situations. On the other hand, the presence of graphene in the high frequency range has an exclusively beneficial effect. Since the VACNT hyperbolic is present albeit weak, the hybridization with graphene allows for improved radiative transfer without the need for extremely deep VACNT substrates. The fascinating properties of graphene uncovered in this recent discussion prove its favorable use in mid-infrared near-field radiative transfer between hyperbolic materials.

IV. CONCLUSIONS

Graphene possesses unique optoelectronic properties that prove to be beneficial additions to near-field radiative heat transfer configurations. Due to their tunable semiconductor-like behavior, a pair of electron-doped graphene sheets separated by a sub-micron vacuum gap allows evanescent wave tunneling in narrowband surface modes (SPP). Due to the intrinsic two hyperbolic bands and a low-frequency surface mode in VACNT, the hybridization with graphene SPP results in quite complex near-field transmission regimes. Graphene SPP does not improve the lower frequency hyperbolic mode, since the latter is supported by the symmetric SPP band of uncovered VACNT. This disruption is especially strong with increased chemical potential in graphene. On the other hand, in the higher frequency hyperbolic band that intrinsically contains fewer hyperbolic modes,

strongly doped graphene allows increased number of near-unity transmission modes due to hybridization. Due to these two competing mechanisms, an optimal chemical potential value for the doped graphene sheets results in the greatest heat flux enhancement over uncovered VACNT. Depending on the frequency of interest, the presence of graphene especially under high doping can drastically increase the penetration depth. The VACNT substrate thickness should be several tens to one hundred micrometers in order to be considered semi-infinite. The sensitivity to graphene doping allows near-field graphene-covered VACNT to be considered as heat flux gating devices or radiative thermal rectifiers. If the attention to near-field radiation is only in the mid-infrared wavelength range and shorter, the mode hybridization with strongly doped graphene is certainly advantageous.

ACKNOWLEDGMENTS

This work was mainly supported by the National Science Foundation (CBET-1235975). XLL was supported by the Department of Energy, Office of Science, Basic Energy Sciences (DE-FG02-06ER46343).

[1] Z. M. Zhang, *Nano/Microscale Heat Transfer* (McGraw-Hill, New York, 2007).
[2] S. Basu, Z. M. Zhang, and C. J. Fu, Int. J. of Energy Res. **33**(13), 1203 (2009).
[3] S. A. Biehs, E. Rousseau, and J. J. Greffet, Phys. Rev. Lett. **105**(23), 234301 (2010).
[4] M. Laroche, R. Carminati, and J.-J. Greffet, J. of Appl. Phys. **100**(6) (2006).
[5] A. Narayanaswamy and G. Chen, Appl. Phys. Lett. **82**(20), 3544 (2003).
[6] K. Park, S. Basu, W. P. King, and Z. M. Zhang, J. Quant. Spect. Rad. Trans. **109**(2), 305 (2008).
[7] P. Ben-Abdallah and S.-A. Biehs, Phys. Rev. Lett. **112**(4), 044301 (2014).
[8] S. Basu and M. Francoeur, Appl. Phys. Lett. **98**(11) (2011).
[9] A. Poddubny, I. Iorsh, P. Belov, and Y. Kivshar, Nat. Photon. **7**(12), 948 (2013).
[10] S. A. Biehs, M. Tschikin, and P. Ben-Abdallah, Phys. Rev. Lett. **109**(10), 104301 (2012).
[11] B. Liu and S. Shen, Phys. Rev. B **87**(11), 115403 (2013).
[12] Y. Guo, C. L. Cortes, S. Molesky, and Z. Jacob, Appl. Phys. Lett. **101**(13) (2012).
[13] S. Lang, M. Tschikin, S.-A. Biehs, A. Y. Petrov, and M. Eich, Appl. Phys. Lett. **104**(12) (2014).
[14] X. Liu, R. Z. Zhang, and Z. Zhang, ACS Photon. **1**(9), 785 (2014).
[15] R. Z. Zhang and Z. M. Zhang, J. Quant. Spec. Rad. Trans., In press (2015).
[16] K. S. Novoselov, A. K. Geim, S. V. Morozov, D. Jiang, Y. Zhang, S. V. Dubonos, I. V. Grigorieva, and A. A. Firsov, Science **306**(5696), 666 (2004).
[17] P. Tassin, T. Koschny, and C. M. Soukoulis, Science **341**(6146), 620 (2013).
[18] A. K. Geim and K. S. Novoselov, Nat. Mater. **6**(3), 183 (2007).
[19] A. Vakil and N. Engheta, Science **332**(6035), 1291 (2011).
[20] K. I. Bolotin, K. J. Sikes, Z. Jiang, M. Klima, G. Fudenberg, J. Hone, P. Kim, and H. L. Stormer, Sol. St. Comm. **146**(9–10), 351 (2008).
[21] Z. Q. Li, E. A. Henriksen, Z. Jiang, Z. Hao, M. C. Martin, P. Kim, H. L. Stormer, and D. N. Basov, Nat. Phys. **4**(7), 532 (2008).
[22] L. A. Falkovsky, J. of Phys.: Conf. Ser. **129**(1), 012004 (2008).
[23] Y. W. Tan, Y. Zhang, K. Bolotin, Y. Zhao, S. Adam, E. H. Hwang, S. Das Sarma, H. L. Stormer, and P. Kim, Phys. Rev. Lett. **99**(24), 246803 (2007).
[24] Y. Zhang, Y.-W. Tan, H. L. Stormer, and P. Kim, Nature **438**(7065), 201 (2005).
[25] K. F. Mak, M. Y. Sfeir, Y. Wu, C. H. Lui, J. A. Misewich, and T. F. Heinz, Phys. Rev. Lett. **101**(19), 196405 (2008).
[26] X. Li, W. Cai, J. An, S. Kim, J. Nah, D. Yang, R. Piner, A. Velamakanni, I. Jung, E. Tutuc, S. K. Banerjee, L. Colombo, and R. S. Ruoff, Science **324**(5932), 1312 (2009).
[27] C. R. Dean, A. F. Young, I. Meric, C. Lee, L. Wang, S. Sorgenfrei, K. Watanabe, T. Taniguchi, P. Kim, K. L. Shepard, and J. Hone, Nat. Nano. **5**(10), 722 (2010).
[28] P.-Y. Chen and A. Alù, ACS Nano **5**(7), 5855 (2011).
[29] Z. Fang, Y. Wang, A. E. Schlather, Z. Liu, P. M. Ajayan, F. J. García de Abajo, P. Nordlander, X. Zhu, and N. J. Halas, Nano Lett. **14**(1), 299 (2013).
[30] W. Gao, G. Shi, Z. Jin, J. Shu, Q. Zhang, R. Vajtai, P. M. Ajayan, J. Kono, and Q. Xu, Nano Lett. **13**(8), 3698 (2013).
[31] C.-H. Liu, Y.-C. Chang, T. B. Norris, and Z. Zhong, Nat. Nano. **9**(4), 273 (2014).
[32] R. Rao, G. Chen, L. M. R. Arava, K. Kalaga, M. Ishigami, T. F. Heinz, P. M. Ajayan, and A. R. Harutyunyan, Sci. Rep. **3** (2013).
[33] Y.-S. Kim, K. Kumar, F. T. Fisher, and E.-H. Yang, Nanotechnology **23**(1), 015301 (2012).
[34] G. K. Dimitrakakis, E. Tylianakis, and G. E. Froudakis, Nano Lett. **8**(10), 3166 (2008).
[35] F. Du, D. Yu, L. Dai, S. Ganguli, V. Varshney, and A. K. Roy, Chem. Mater. **23**(21), 4810 (2011).
[36] J. Lee, V. Varshney, J. S. Brown, A. K. Roy, and B. L. Farmer, Appl. Phys. Lett. **100**(18) (2012).
[37] Y. Xu, K. T. He, S. W. Schmucker, Z. Guo, J. C. Koepke, J. D. Wood, J. W. Lyding, and N. R. Aluru, Nano Lett. **11**(7), 2735 (2011).
[38] M. Lim, S. S. Lee, and B. J. Lee, Opt. Ex. **21**(19), 22173 (2013).
[39] M. Jablan, H. Buljan, and M. Soljačić, Phys. Rev. B **80**(24), 245435 (2009).

[40] K. Nomura and A. H. MacDonald, Phys. Rev. Lett. **98**(7), 076602 (2007).
[41] W. Zhu, V. Perebeinos, M. Freitag, and P. Avouris, Phys. Rev. B **80**(23), 235402 (2009).
[42] L. A. Falkovsky and S. S. Pershoguba, Phys. Rev. B **76**(15), 153410 (2007).
[43] S. A. Mikhailov and K. Ziegler, Phys. Rev. Lett. **99**(1), 016803 (2007).
[44] F. J. García-Vidal, J. M. Pitarke, and J. B. Pendry, Phys. Rev. Lett. **78**(22), 4289 (1997).
[45] R. Z. Zhang, X. Liu, and Z. M. Zhang, J. Heat Trans. In press (2015).
[46] B. T. Draine and H. M. Lee, Astrophys. J. **285**(1), 89 (1984).
[47] T. de los Arcos, M. G. Garnier, P. Oelhafen, J. W. Seo, C. Domingo, J. V. García-Ramos, and S. Sánchez-Cortés, Phys. Rev. B **71**(20), 205416 (2005).
[48] X. J. Wang, J. D. Flicker, B. J. Lee, W. J. Ready, and Z. M. Zhang, Nanotech. **20**(21), 215704 (2009).
[49] S. Basu and L. Wang, Appl. Phys. Lett. **102**(5) (2013).
[50] H. Ye, X. J. Wang, W. Lin, C. P. Wong, and Z. M. Zhang, Appl. Phys. Lett. **101**(14), 141909 (2012).
[51] R. Messina and P. Ben-Abdallah, Sci. Rep. **3**, 1383 (2013).
[52] B. Wang, X. Zhang, X. Yuan, and J. Teng, Appl. Phys. Lett. **100**(13) (2012).
[53] E. H. Hwang and S. Das Sarma, Phys. Rev. B **75**(20), 205418 (2007).
[54] C. H. Gan, H. S. Chu, and E. P. Li, Phys. Rev. B **85**(12), 125431 (2012).
[55] X. L. Liu, R. Z. Zhang, and Z. M. Zhang, Appl. Phys. Lett. **103**(21) (2013).
[56] O. Ilic, M. Jablan, J. D. Joannopoulos, I. Celanovic, H. Buljan, and M. Soljačić, Phys. Rev. B **85**(15), 155422 (2012).
[57] M. Jablan, M. Soljacic, and H. Buljan, Proc. IEEE **101**(7), 1689 (2013).
[58] P. Rodriguez-Lopez, W.-K. Tse, and D. A. R. Dalvit, arXiv:1410.4387 (2014).
[59] T. J. Bright, X. L. Liu, and Z. M. Zhang, Opt. Ex. **22**(S4), A1112 (2014).
[60] M. Francoeur, M. Pinar Mengüç, and R. Vaillon, J. Quant. Spect. Rad. Trans. **110**(18), 2002 (2009).
[61] J. K. Lee and J. A. Kong, Electromagnetics **3**(2), 111 (1983).
[62] J. E. Sipe, JOSA B **4**(4), 481 (1987).
[63] M. Auslender and S. Hava, Opt. Lett. **21**(21), 1765 (1996).
[64] M. A. K. Othman, C. Guclu, and F. Capolino, Opt. Ex. **21**(6), 7614 (2013).
[65] S. Basu and Z. M. Zhang, Appl. Phys. Lett. **95**(13) (2009).